photonics

Article

Multi-Layered Metamaterial Absorber: Electromagnetic and Thermal Characterization

Bui Xuan Khuyen [1,2], Ngo Nhu Viet [1,3,†], Pham Thanh Son [2], Bui Huu Nguyen [4], Nguyen Hai Anh [1,2], Do Thuy Chi [5], Nguyen Phon Hai [6], Bui Son Tung [1,2,†], Vu Dinh Lam [1], Haiyu Zheng [7,8], Liangyao Chen [9] and Youngpak Lee [7,8,9,*]

[1] Faculty of Materials Science and Energy, Graduate University of Science and Technology, Vietnam Academy of Science and Technology, 18 Hoang Quoc Viet, Hanoi 100000, Vietnam; khuyenbx@ims.vast.ac.vn (B.X.K.); nhuvietnv5@gmail.com (N.N.V.); anhnh@ims.vast.ac.vn (N.H.A.); tungbs@ims.vast.ac.vn (B.S.T.); lamvd@gust-edu.vast.ac.vn (V.D.L.)
[2] Institute of Materials Science, Vietnam Academy of Science and Technology, 18 Hoang Quoc Viet, Cau Giay, Hanoi 100000, Vietnam; sonpt@ims.vast.ac.vn
[3] People's Police Academy, Co Nhue 2, Bac Tu Liem, Hanoi 100000, Vietnam
[4] Department of Physics, Hanoi University of Mining and Geology, 18 Pho Vien, Bac Tu Liem District, Hanoi 100000, Vietnam; buihuunguyen@humg.edu.vn
[5] Faculty of Physics, Thai Nguyen University of Education, Thai Nguyen 250000, Vietnam; chidt@tnue.edu.vn
[6] Air Defence-Air Force Academy, Kim Son, Son Tay, Hanoi 100000, Vietnam; nphai88@gmail.com
[7] Department of Physics, Quantum Photonic Science Research Center and RINS, Hanyang University, Seoul 04763, Republic of Korea; haiyu@hanyang.ac.kr
[8] Alpha ADT, Dongtan Advanced Industrial, No.1202, 51-9, Hwaseong 18469, Republic of Korea
[9] Department of Optical Science and Engineering, Fudan University, Shanghai 200433, China; lychen@fudan.ac.cn
* Correspondence: yplee@hanyang.ac.kr
† These authors contributed equally to this work as co-correspondence.

Abstract: Metamaterials, recognized as advanced artificial materials endowed with distinctive properties, have found diverse applications in everyday life, military endeavors, and scientific research. Starting from monolayer metamaterials, multilayer ones are increasingly researched, especially in the field of electromagnetic wave absorption. In this article, we propose a multilayer metamaterial-absorber (MA) structure comprising two resonant layers crafted with copper and FR-4 dielectric. The presented multilayer MA structure exhibited an absorption greater than 90% in a frequency range from 4.84 to 5.02 GHz, with two maximum absorption peaks at 4.89 and 4.97 GHz. The bandwidth of the multilayer MA surpassed that of the individual single-layer MAs, with extension fractions reaching 360% and 257%, respectively. Through the simulation and calculation, the field distribution and equivalent circuit model elucidated that both individual magnetic resonances and their interplay contribute significantly to the absorption behavior of the multilayer MA. The absorption of the proposed multilayer MA structure was also investigated for the oblique incidence in the transverse electric (TE) and transverse magnetic (TM) modes. In the TE mode, the absorption intensity of two maximum peaks was maintained at over 93% up to an incident angle of 40 degrees and dropped to below 80% at an incident angle of 60 degrees. In the TM mode, the absorption was more stable and not significantly affected by the incident angle, ranging from 0 to 60 degrees. An absorption greater than 97% was observed when the incident angle increased from 0 to 60 degrees in the TM mode. Additionally, the approach in our work was further demonstrated by adding more resonant layers, making 3- and 4-layer structures. The results indicated that the absorption bandwidths of the 3- and 4-layer structures increased by 16% and 33%, respectively, compared to the bilayer structure. Furthermore, we analyzed the thermal distribution within the MA to understand the dissipation of absorbed electromagnetic energy. This research offers valuable insight into the augmented MA through a multilayer structure, presenting the implications for microwave applications like electromagnetic shielding, as well as in the design of MAs for terahertz devices and technologies, including emission and thermal imaging. These findings contribute to the advancement of knowledge in enhancing the absorption capabilities across various frequency ranges, expanding the potential applications of metamaterials.

Citation: Khuyen, B.X.; Viet, N.N.; Son, P.T.; Nguyen, B.H.; Anh, N.H.; Chi, D.T.; Hai, N.P.; Tung, B.S.; Lam, V.D.; Zheng, H.; et al. Multi-Layered Metamaterial Absorber: Electromagnetic and Thermal Characterization. *Photonics* **2024**, *11*, 219. https://doi.org/10.3390/photonics11030219

Received: 1 February 2024
Revised: 24 February 2024
Accepted: 26 February 2024
Published: 28 February 2024

Keywords: multilayer; metamaterial absorber; thermal distribution

1. Introduction

Metamaterials are artificial materials formed by arranging material structures according to certain rules; from there, many interesting physical properties that do not exist in nature can be obtained, for example, negative refractive index [1,2] asymmetric transmission [3,4], cross-polarization conversion [5,6], and perfect absorption [7,8]. According to previous research on metamaterial absorbers (MAs), there have been more studies on absorbers [9], ranging from the microwave [10,11] to the terahertz [12–14], infrared, and even visible regions, achieving perfect absorption [15,16], polarization insensitivity [17–20], wide incidence angle [21–23], and adjustable absorption [24–26].

Starting from monolayer metamaterials, multilayer metamaterials are increasingly being researched, especially in the field of electromagnetic wave absorption. For example, a three-layer MA with multiple perfect absorptions, consisting of a bisected square ring, was proposed by Liu et al. [27]. The number of absorption peaks could be adjusted from three to five and the absorption frequency range could be expanded, leading to a broadband resonance by increasing the number of layers. Liu et al. also suggested a multilayer metal–dielectric grating, consisting of a multilayer nickel–silicon nitride (Ni-SiN) grating on a metallic Ni substrate, as a broadband near-perfect absorber [28]. This multilayer metamaterial had an absorption of 99.24% in a wavelength range of 400–2000 nm. Quan et al. investigated a broadband infrared stealth metamaterial absorber, based on an innovative metal–dielectric–metal structure whose top pattern consisted of multiple layers [29]. The structure employed high-temperature resistant materials instead of traditional low melting-point precious metals and achieved selective heat radiation in the infrared range. As the number of layers increased, the absorption peak and bandwidth of the non-atmospheric window band broadened. Gandhi et al. presented the design of a polarization-independent broadband absorber in a THz frequency range using a metasurface resonator [30]. The absorber was composed of three layers, whose top layer was made with a vanadium–dioxide resonator of a conductivity σ = 200,000 S/m. The bottom layer consisted of flat layers made of gold metal and a dielectric layer sandwiched between the two layers. The optimized absorber exhibited an absorption greater than 90% in 2.54–5.54 THz. Liu et al. introduced a multilayer graphene structure. The optimized device showed an absorption of over 90% in a bandwidth between 1.12 and 3.78 THz [31]. An alternative approach included many resonant meta-atoms in the same plane, instead of stacking them vertically [32]. This has an advantage when one plane is employed for the metamaterial structure; however, the structure also becomes more complicated.

In this paper, we numerically and experimentally investigate a broadband MA based on a multilayer structure. The proposed multilayer MA structure has identical resonator layers, which show a broader absorption bandwidth in comparison to that of the individual single-layer absorber. Our research focuses on clarifying the interaction between metal layers, as well as the absorption mechanism through the simulated field distribution and the calculated equivalent circuit model. Furthermore, the temperature distribution is also presented to reveal the energy dissipation in MA.

2. Multilayer Metamaterial Structures and Methods

The unit cell structures of the single-layer and multilayer Mas operating in the GHz-frequency region are depicted in Figure 1. The single-layer MA was composed of a metal–dielectric layer, placed on a continuous metal layer, with a unit cell size of a. The multilayer MA was made by increasing the number of metal–dielectric layers. In the metal–dielectric layer, the metallic part was patterned with a plus-shaped structure with a thickness of t_m, length of b, and width of c, and placed on a continuous dielectric with a thickness of t_d. The bottom continuous metallic sheet had a thickness of t_b. The structural parameters of the unit cell were set at a = 18, b = 16, c = 7, t_b = 0.035, and t_m = 0.035 mm. In our investigation, the dielectric was FR-4 with a permittivity of 4.3 and a loss tangent of 0.025. The metal layers were made of copper with a conductivity of 5.96×10^7 S/m.

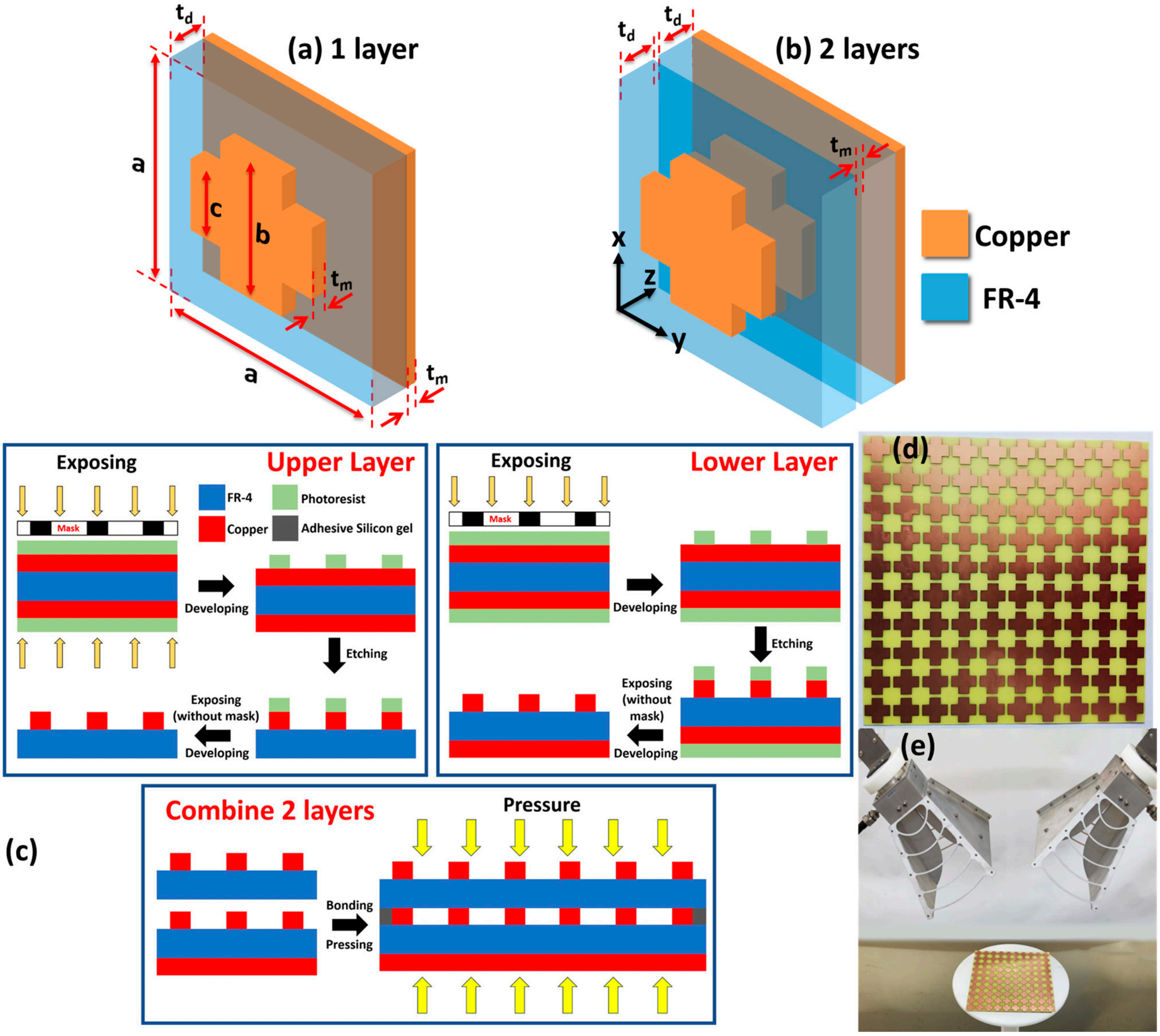

Figure 1. MA of the (**a**) single- and (**b**) two-layer structures. (**c**) Fabrication process of bilayer metamaterial. (**d**) Fabricated sample and (**e**) schematic of the experimental configuration.

The single-layer and multilayer MAs were designed to elucidate the electromagnetic properties by using CST Microwave Studio 2023 software. There Maxwell's equations describe the interaction between electromagnetic waves and materials, which was solved by the finite integration technique. In the simulation, the incident wave is a plane wave with the wave vector, k, placed perpendicular to the MA surface, and the **E–H** plane parallel to the structure surface. The periodic boundary conditions were established for the unit cells in the x and y axes (**E–H** plane). The z-direction was open. The main simulation results included the reflection parameter, S_{11}, and transmission one, S_{21}. The absorption of the MA, denoted as $A(\omega)$, was calculated by using the following formula:

$$A(\omega) = 1 - R(\omega) - T(\omega), \tag{1}$$

where $R(\omega) = |S_{11}|^2$ is the reflection and $T(\omega) = |S_{21}|^2$ is the transmission.

To demonstrate the electromagnetic properties of the proposed multilayer MA, a sample with 10 × 10 unit cells was fabricated on an FR-4 substrate. In this study, the multilayer MA was prepared layer-by-layer, based on photolithography. The fabricated single layers were tightly bonded together and placed on a continuous metal layer. To bond two single layers together, we used silicon gels on the four outer edges of the two layers and then pressing and vacuum techniques. It helps that the silicon gel has nearly no effect on the electromagnetic properties of the metamaterial slab. Figure 1c presents the schematic of the fabrication process with detailed steps. Figure 1d shows a photograph of the fabricated sample with the overall dimensions of 180 × 180 mm^2. We employed copper for the resonant layers at the top and the continuous layer at the bottom. The absorption properties of the fabricated multilayer MA were measured in the free space. We used a vector-network analyzer system to measure the S parameters in Figure 1e.

In the experimental configuration, owing to the copper-backed layers, the absorption was reduced and determined by an equation denoted as $A = 1 - |S_{11}|^2$, where S_{11} signifies the theoretically defined scattering parameter corresponding to the reflection wave. To calculate the S_{11} coefficient within our free-space measurement configuration, we employed horn linearly polarized standard-gain antennas. The horn antennas were placed on the same side relative to the sample plane to measure the reflection wave from the MA sample. Additionally, owing to the physical size of the antenna, the reflection could not be measured exactly at the normal incidence. Hence, the antennas were arranged so that the incident angle was approximately 10°, which, despite its deviation, was considered as an approximate condition of the normal incidence.

In the calibration process, which was necessary for our measurement setup, a copper plate, mirroring the dimensions of the absorber, served as a reference standard. The copper plate was postulated to be a perfect reflector and positioned at the identical position as the MA sample in the testing environment. The calibration was achieved by deriving the reference signal from the measured electromagnetic wave reflection off the copper plate, which was considered a perfectly reflecting body in this context. This reference signal was a benchmark for the reflection from the real MA samples. By normalizing the reflection signal from the MA sample and that from the copper plate (reference signal), the reflection coefficient was estimated precisely, thereby providing an elucidation of the absorption characteristics of the proposed MA structure.

3. Results and Discussion

The absorption spectra of the proposed multilayer MA structure and single layer are shown in Figure 2. The results show that the two single-layer MAs (t_d = 0.35 and 0.735 mm, respectively) have absorption peaks at 5.02 and 4.93 GHz with absorption values of 94.79% and 95.12%, respectively. Since the backed-copper plate is present in the MA configuration, the effective impedance of the MA is calculated as follows [33]:

$$Z(\omega) = \sqrt{\frac{(1 + S_{11}(\omega))^2 - {S_{21}}^2(\omega)}{(1 - S_{11}(\omega))^2 - {S_{21}}^2(\omega)}} = \sqrt{\frac{(1 + S_{11}(\omega))^2}{(1 - S_{11}(\omega))^2}}. \quad (2)$$

The multilayer MA structure provides the absorption spectrum with an absorption greater than 90% in a frequency range of 4.84–5.02 GHz, as seen in Figure 2a. There are two maximum absorption peaks at 4.89 and 4.97 GHz with absorption values of 98.99% and 98.44%, respectively. Compared to the single-layer MAs, the bandwidth with an absorption value above 90% turns out to be broader (360% and 257%, respectively) than that of single-layer MA corresponding to t_d = 0.35 and 0.735 mm. The absorption mechanism of the MA works by reducing the reflection through the impedance matching with the surrounding air. Figure 2b shows the impedance matching of the multilayer MA at the resonant frequencies. The relative impedance is close to 0.9, so the reflection of the electromagnetic wave is negligible. In addition, the impedance spectra of single-layer MAs with t_d = 0.35 and 0.735 mm were also investigated, as seen in Figure 2c,d.

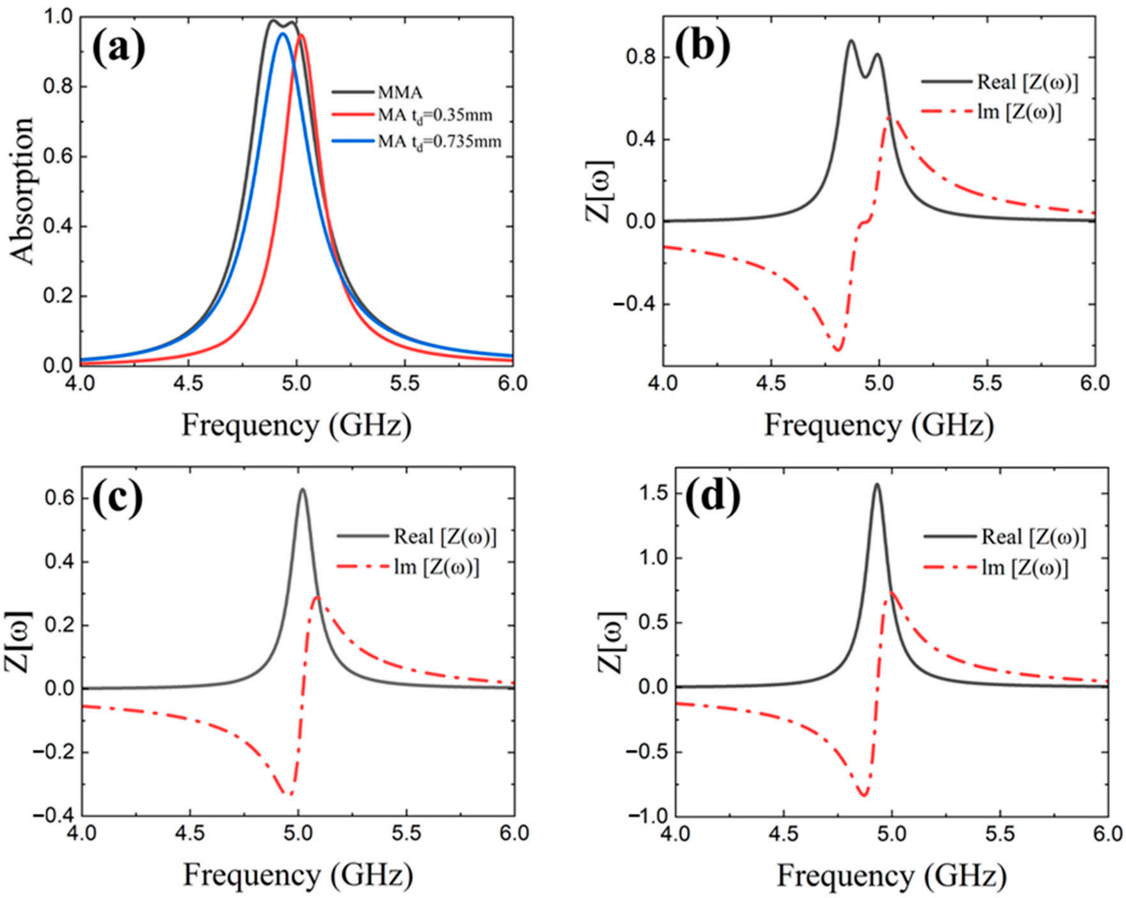

Figure 2. (**a**) Absorption spectra of the multilayer MA and single-layer ones with two different dielectric layer thicknesses. (**b**) Effective impedance of the multilayer MA, and single-layer ones with t_d = (**c**) 0.35 and (**d**) 0.735 mm.

To clarify the interaction between metallic layers, the current and magnetic field distributions were also investigated. Figure 3 presents the surface current distributions at different phases at the resonance frequencies of 4.97 and 4.89 GHz of the multilayer MA. The results show that the surface currents on the metallic layers are in opposite directions, which shows that magnetic resonance occurs between those layers. Figure 4a–d reveal that the high-intensity anti-parallel currents appear mainly between the upper plus-shaped metallic layers at 4.97 GHz. At a phase of 160°, the surface current between the two plus-shaped metallic layers reaches the maximum intensity, as shown in Figure 3c. In addition, the anti-parallel surface currents are also observed between the middle plus-shaped layer and the bottom continuous one. However, these currents are not in phase and their intensities are much weaker in comparison to those on two plus-shaped layers.

The surface current distribution between the metallic layers at 4.89 GHz is shown in Figure 3e–h). A greater surface current density appears on the surface of the middle plus-shape layer and the bottom continuous one. At the zero phase and a phase of 180°, the maximum magnetic resonance is revealed between the two lower metallic layers, as seen in Figure 3e,h. The surface current density between the two upper layers reaches the maximum at the zero phase and a phase of 180°. The phase delay is also noticed between the anti-parallel currents induced on two pairs of copper layers (top-middle and middle-bottom layers). In comparison with the surface current distribution at the absorption frequency of 5.02 GHz of the single-layer MA with t_d = 0.35 mm [Figure 3i–n], the phase reversal time of the currents becomes longer. The induced current reverses the phase in phase intervals of approximately 90° and 180° for the single-layer and multilayer structures, respectively.

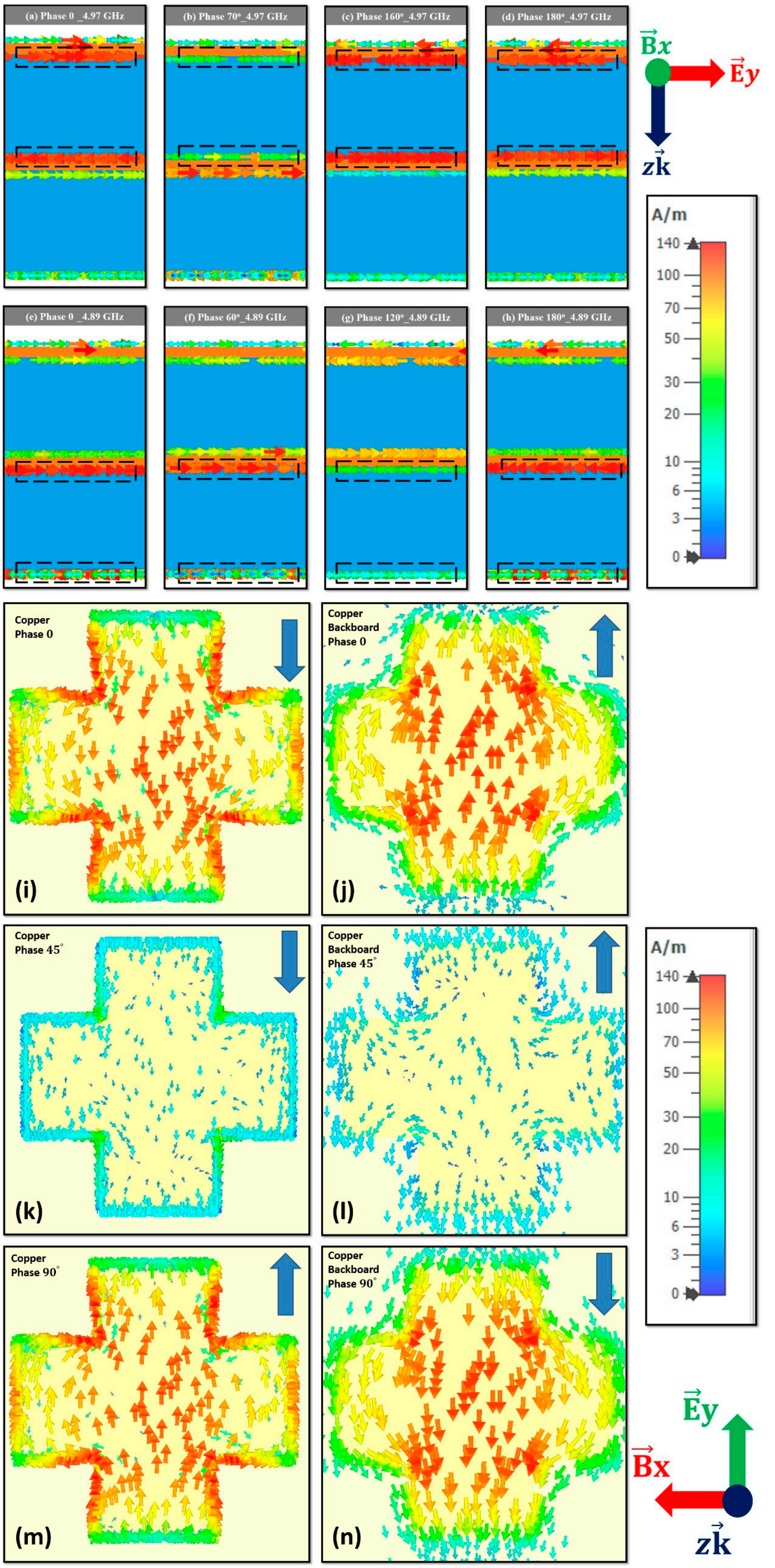

Figure 3. Surface current distributions at (**a**–**d**) 4.97 and (**e**–**h**) 4.89 GHz of the multilayer MA. (**i**–**n**) Surface current distributions at 5.02 GHz of single-layer MA.

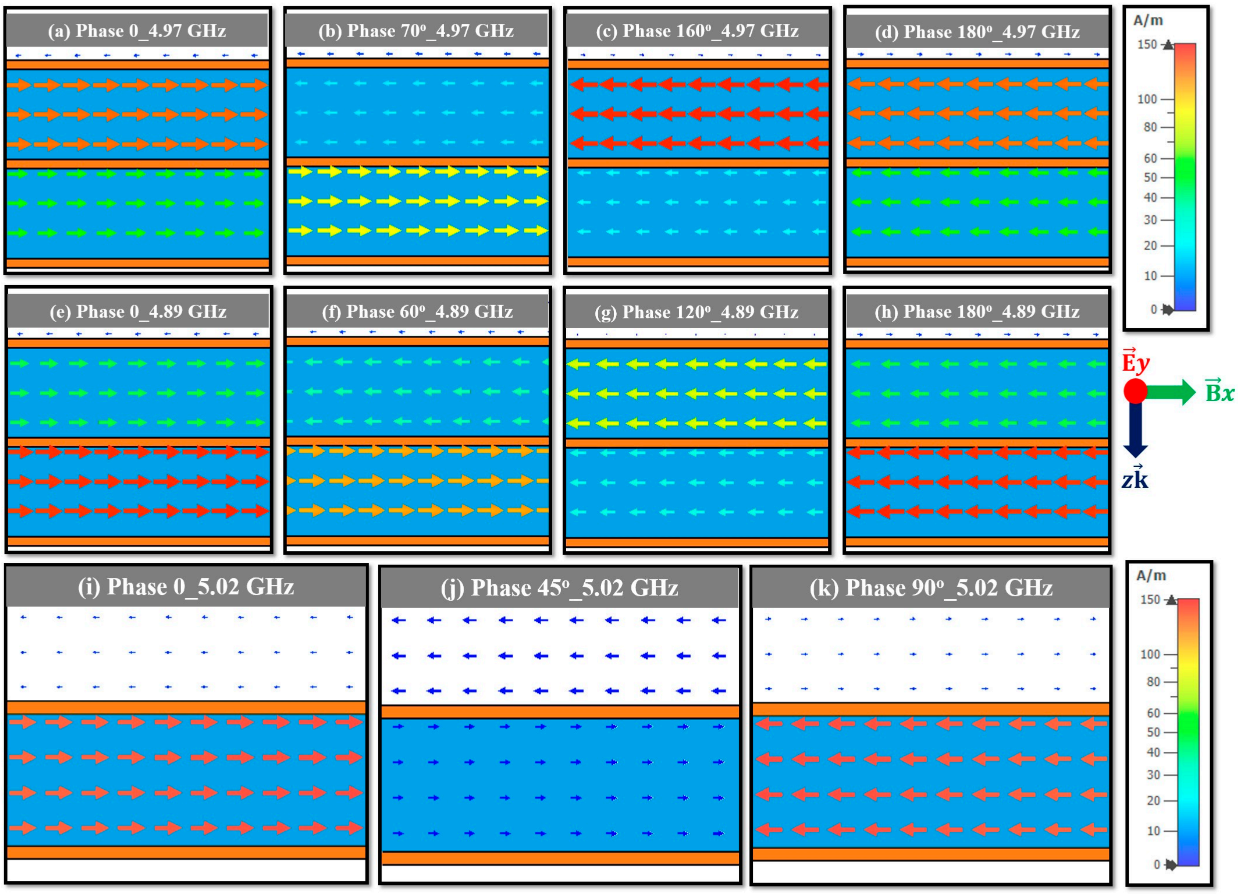

Figure 4. Magnetic field distributions at (**a**–**d**) 4.97 and (**e**–**h**) 4.89 GHz of the multilayer MA. (**i**–**k**) Magnetic field distributions at 5.02 GHz of the single-layer MA.

To better visualize the magnetic resonances at the absorption frequencies, the magnetic field distribution was investigated. Figure 4 shows that the induced magnetic field appears between the plus-shaped metallic layers, and between the middle plus-shaped metallic layer and the bottom continuous one. At 4.97 GHz, a strong magnetic field is induced between the top and middle copper layers, as shown in Figure 4a–d. The magnetic field with weaker intensity and delayed phase is also observed between the middle and bottom copper layers. On the other hand, at 4.89 GHz, there is a higher-intensity magnetic field concentrated between the middle and bottom copper layers, and a weaker and phase-delayed magnetic field between the top and middle copper ones. The induced magnetic field distribution is consistent with the surface currents reported in Figure 3. Similarly, in comparison to the magnetic field distribution at the absorption frequency of the single-layer MA with t_d = 0.35 mm [Figure 4i–k], the induced magnetic field of the multilayer structure reverses the direction over a phase interval of 180 degrees, which is nearly twice that of the single-layer one.

The simulated anti-parallel surface currents and magnetic fields suggest that the absorption peaks of the MA are relevant to the magnetic resonances induced between copper layers. When passing through and interacting with each metallic layer, a phase delay appears in the z direction, thereby leading to a phase shift in the magnetic resonance in each pair of layers.

To quantitatively confirm that the absorption is led by the magnetic interaction between the metallic layers, we established the copper connectors between the copper layers. The connectors eliminated the effective capacitance in the LC model, leading to the suppression of magnetic resonance. In the case of an additional bridging system installed between different layers, the absorption spectrum was obtained for each case shown in

Figure 5. When the top and middle layers are connected, an absorption peak appears at 4.89 GHz. By connecting the middle and bottom layers, the maximum absorption peak is shown at a frequency of 4.97 GHz. The absorption peaks are extinguished completely when all metallic layers are connected. This indicates that the absorption of the multilayer MA is caused by the interlayer magnetic resonance. The interaction between the middle plus-shape layer and the bottom continuous one results in a resonance peak at 4.89 GHz. This—between the two plus layers—leads to a resonance peak at 4.97 GHz. We note that, in this structure, the gap width is large (2 mm) so the horizontal capacitance between the crosses has a very small effect on the overall frequency response of the structure. Therefore, this capacitance value can be ignored in our model [34].

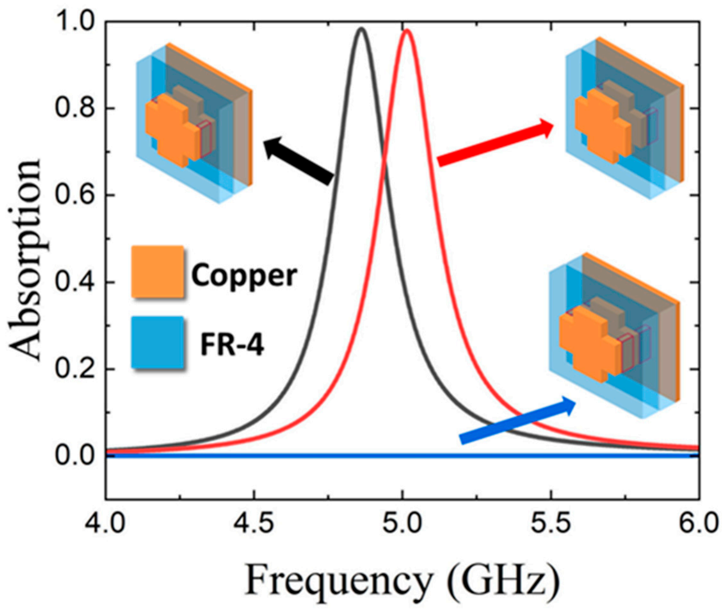

Figure 5. Absorption spectra of the multilayered MA when additional connectors are installed between layers: the top and middle layers (black-solid line), the middle and bottom ones (red-solid line) and all metallic ones (blue-solid line).

Figure 6 shows the equivalent-circuit model for the proposed multilayer structure. From the geometry of the plus-shaped structure, the inductance coefficient of loop L_i can be calculated as follows [34]:

$$L_i = \frac{L}{2} = \frac{\mu l t_i}{2w}, \tag{3}$$

where l is the length of the plus-shaped metallic wire, t_i is the thickness of the dielectric pad, w is the width of the plus-shaped metallic wire, and μ denotes free-space permeability.

$$C_i = \varepsilon_0 \varepsilon c_1 \frac{s_i}{t}, \tag{4}$$

$$f_i = \frac{1}{2\pi\sqrt{L_i C_i}}, \tag{5}$$

where c_1 is a geometrical factor of $0.2 \leq c_1 \leq 0.3$ [29], s_i is the area of the plus shape, ε_0 is the free-space permittivity, and ε is the permittivity of FR-4. The calculational results are shown in Figure 6b. They are in good agreement with the simulation of the proposed multilayer MA.

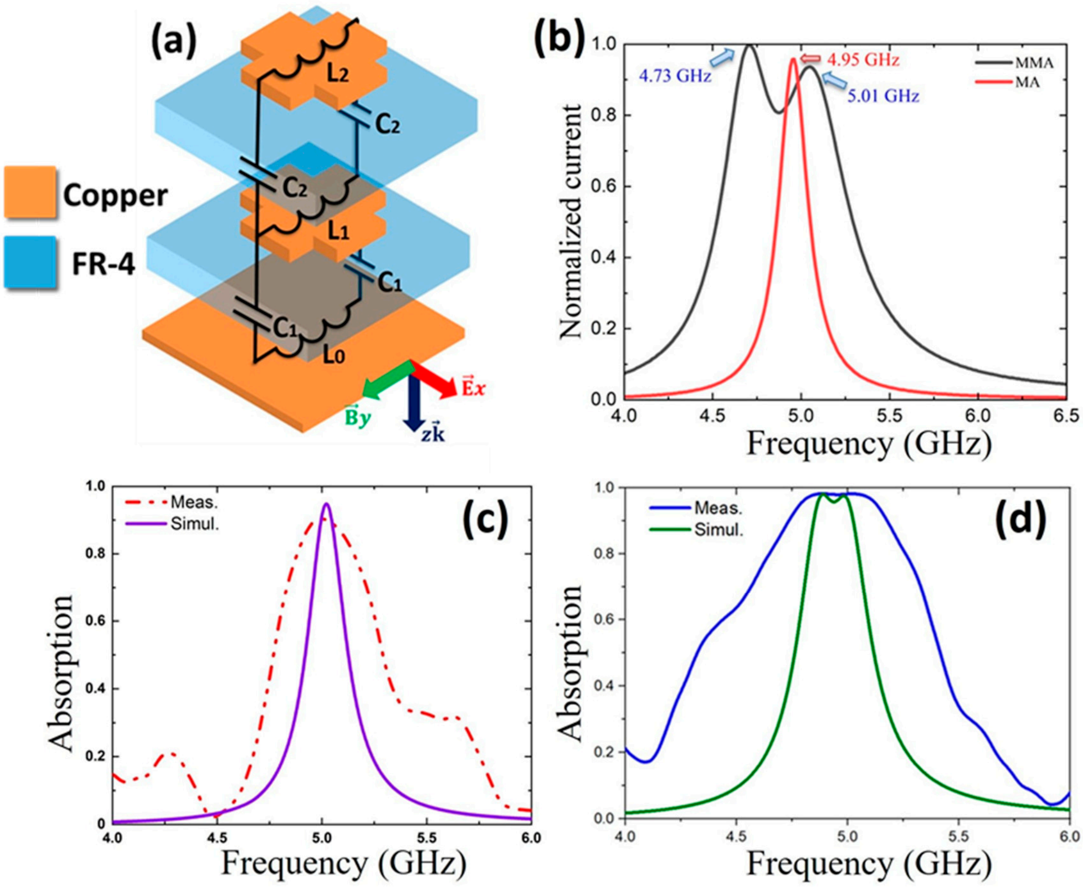

Figure 6. (**a**) Equivalent-circuit models of the multilayer MA. (**b**) Calculation of the normalized total current in the single and multilayer MAs, according to the LC circuit model. Measured and simulated absorption spectra of (**c**) the single-layer and (**d**) multilayer MA.

The equivalent-circuit model can be divided into two resonant loops linked to each other through the coupling coefficient, k. Therefore, the mutual coupling, M, is calculated according to the following formula:

$$M_{10} = k_1\sqrt{L_1 L_0}, \tag{6}$$

$$M_{21} = k_2\sqrt{L_2 L_1}. \tag{7}$$

In a resonant circuit, the direction of the electromagnetic wave traveling from L_2 through L_1 to L_0, results in the coupling effect on the oscillating circuit being opposite for the two circuits (L_2 to L_1 and L_1 to L_0). This is shown by the signs of M_{10} and M_{21} in the equation used to calculate the resonance frequency. The value of coupling in this case is quite small, which makes the frequencies of the two circuits only slightly different, as in the calculation and simulation.

$$f_1 = \frac{1}{2\pi\sqrt{((L_1 - M_{10}) + L_0)(C_1 + C_1)}}, \tag{8}$$

$$f_2 = \frac{1}{2\pi\sqrt{((L_1 + M_{21}) + L_2)(C_2 + C_2)}}. \tag{9}$$

The Kirchoff's equations are built from an electric circuit:

$$\begin{cases} \left(R_2 + j\omega L_2 + \frac{1}{j\omega C_2}\right) I_2 - j\omega k_{21}\sqrt{L_2 L_1 I_1} = V \\ \left(R_1 + j\omega L_0 + \frac{1}{j\omega C_1}\right) I_1 - j\omega k_{10}\sqrt{L_1 L_0 I_2} = 0 \end{cases}. \tag{10}$$

By solving the above equations, we have the currents in the sub-circuits corresponding to each layer:

$$\begin{cases} I_2 = \frac{R_2}{R_1R_2+\omega^2 k_{10}k_{21}L_1\sqrt{L_0L_2}}V \\ I_1 = \frac{j\omega k_{10}\sqrt{L_1L_0}I_2}{R_1+j\omega L_0+\frac{1}{j\omega C_1}} \end{cases}. \quad (11)$$

The absorption spectrum in MA is proportional to the induced current, which is the total consumption of currents in the sub-circuits. Figure 6b presents the calculated spectrum of the total current of the circuit model for MA and multilayer MA. In the case of the MA, a sharp peak appears at 4.95 GHz. On the other hand, for the multilayer MA configuration, the shape of the current spectrum is consistent with that of the absorption spectrum, which shows two peaks at 4.73 and 5.01 GHz.

The comparisons of the absorption spectra between the single-layer and multilayer MAs in the experiment and simulation are presented in Figure 6c,d. For the single layer, the simulated and experimental results show single peaks at 5.02 and 5.00 GHz with absorption values of 94.7% and 90.3%, respectively. For the multilayer MA, in the simulation, the absorption reaches greater than 90% in a frequency range of 4.84–5.02 GHz. The experimental absorption is 90% in a wider frequency range of 4.72–5.18 GHz. Therefore, the simulated and experimental full-width results at the half-maximum of the absorption of the multilayer MA are 163% and 200% broader than those of the single-layer MA, respectively. The discrepancy between the simulation and experiment might be due to errors in the fabrication of the sample. There are unexpected factors that might lead to the difference between the simulated and experimental results, such as the small size discrepancy between resonators in different layers during the photolithography process, or the slight misalignment between layers during the layer-bonding process.

Various types of electromagnetic waves with diverse incidence angles permeate the environment. Consequently, we investigated the absorption characteristics of the multilayer MA for different incident angles. Figure 7 illustrates the absorption performance of the proposed multilayer MA for the incident-wave angle in both transverse electric (TE) and transverse magnetic (TM) modes. Figure 7a delineates the absorption behavior of the multilayer MA in the TE mode by varying the incidence angle. Notably, in the TE mode, the change in the incidence angle exhibits a minimum frequency shift, with a slight drop in the absorption as the incident angle (θ) varies from 0 to 20°. At 20°, the absorption peaks reach 98% and 97%. Subsequently, at 40°, the absorptions are reduced slightly to 94% and 93%, respectively. Further, when the incident angle reaches 60°, the absorption remains below 80%, that is, 80% and 79%, respectively. Conversely, in the TM mode (depicted in Figure 7b), it is interesting that the absorption and the frequencies turn out to be more stable according to the incident angle, compared to the TE mode. For instance, at θ = 40° and 60°, the two peaks show absorptions of 97% and 99%, and 98% and 99%, respectively. The stable absorption in the TM mode can be understood by the magnetic resonances, which are maintained well since the oblique incidence does not change the direction of the incident magnetic field in the TM mode.

To further clarify the enhancement of the absorption bandwidth by adding more layers, the absorption spectrum was simulated by increasing the number of resonator layers, as shown in Figure 8. The parameters of the 3- and 4-layer structures are identical to those of the proposed bilayer structure. However, to optimize the absorption itself and the absorption bandwidth, the thickness of the dielectric layer, denoted as t_d, was adjusted to 0.3 mm for the 3-layer structure and 0.25 mm for the 4-layer one. The absorber consisting of two layers exhibits an absorption bandwidth ranging from 4.84 to 5.02 GHz, with the absorption exceeding 90%. Upon changing to three layers, the absorption bandwidth with absorption exceeding 90% expands to 4.68–4.89 GHz, indicating a 16% increase compared to the bilayer configuration. With 4 layers, the absorption bandwidth extends further, ranging from 4.65 to 4.89 GHz, marking a 33% increase compared to the bilayer structure, and the absorption is maintained at greater than 90%. This study demonstrates that the broad absorption bandwidth of material is attributed to the interlayer interactions.

Consequently, augmenting the number of layers also enhances the absorption bandwidth of multilayer metamaterial, compared to previous works related to the multilayer MA, which are commonly composed of progressively different-sized resonators or resonators of different shapes [28,31]. In this study, we propose a simple multilayer MA operating in the GHz frequency region with identically shaped/sized resonators, which are easier to manufacture. Although the absorption bandwidth was relatively narrow, widening the absorption bandwidth can also be achieved by increasing the number of layers in the MA structure.

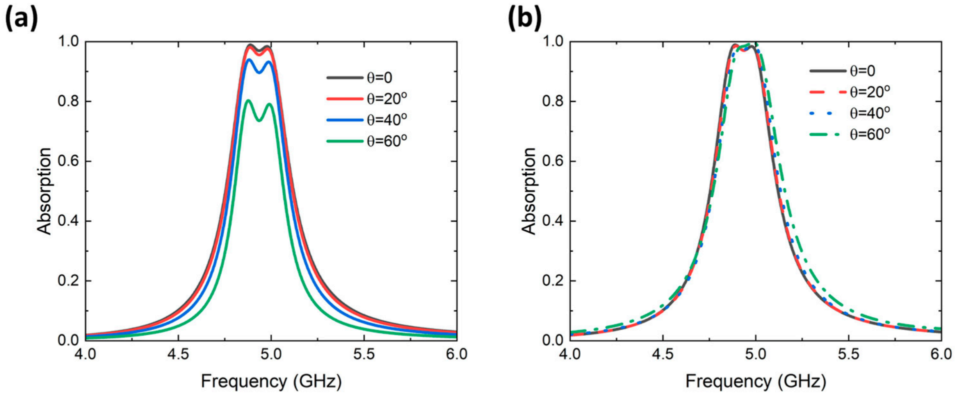

Figure 7. Evolution of the absorption spectrum of the MA structure at different incidence angles in the (**a**) TE and (**b**) TM modes.

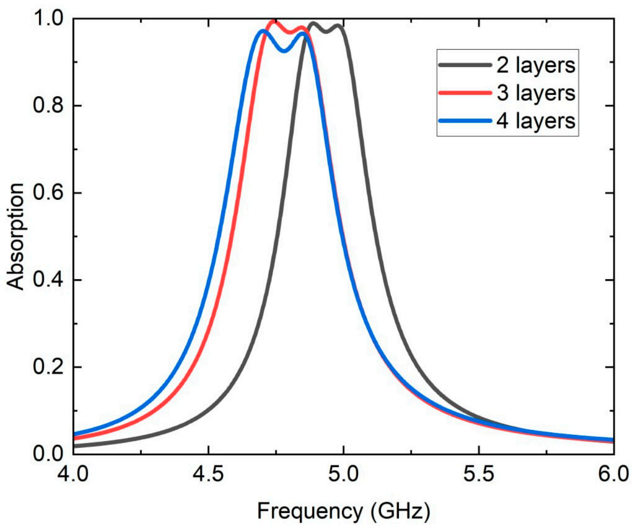

Figure 8. Evolution of the absorption spectrum of the MA structure according to the number of layers.

In the microwave region, the absorbed energy in MA is commonly dissipated as thermal energy through dielectric loss. To further understand, the thermal distributions in MA were simulated and characterized. The input power of 0.1 W was utilized in the simulation. The periodic boundary conditions were assigned to the side face pairs. As a result, the following conditions were satisfied on the four sides of the unit cell: $\partial T/\partial n = 0$. This led to no heat transfer across the boundaries. However, the coupled EM–thermal simulation in CST did not support the periodic boundary conditions for heat transfer. Therefore, the adiabatic conditions were employed as a substitute to ensure that there was no heat flux across the boundaries. The upper surface was designated as open. The lower one was assigned to follow the adiabatic boundary condition due to the placement of the sample on a thermal insulation base. The heat loss generated by the electromagnetic wave increased the temperature of the MA. The steady-state heat distribution is given by the equations below [35]:

$$\Delta \cdot (-\kappa \Delta t) = Q_{ext}, \tag{12}$$

$$Q_{ext} = \frac{1}{2} Re\left[(\sigma - j\omega\varepsilon)\boldsymbol{E} \cdot \boldsymbol{E}^{*}\right]. \tag{13}$$

where κ is the thermal conductivity, Q_{ext} is the heat source produced by the electromagnetic wave [36], and σ denotes electrical conductivity. Natural convective heat flux occurs on the upper surface, $q_{conv} = h(T - T_0)$. Here, $h = 5$ W/m^{2}K, K is the heat convection coefficient and T_0 is the ambient temperature, which is 20 °C. The adiabatic boundary conditions were applied to the other surfaces. The temperature distribution is depicted in Figure 9. The maximum temperatures observed on the surface, corresponding to the frequencies of 4.89 and 4.97 GHz, are 38.67 °C and 38.75 °C, respectively. Since the absorption is induced by the magnetic resonance, the temperatures are the highest at the ends of the plus resonators, corresponding to the positions of the effective capacitances of the magnetic resonances.

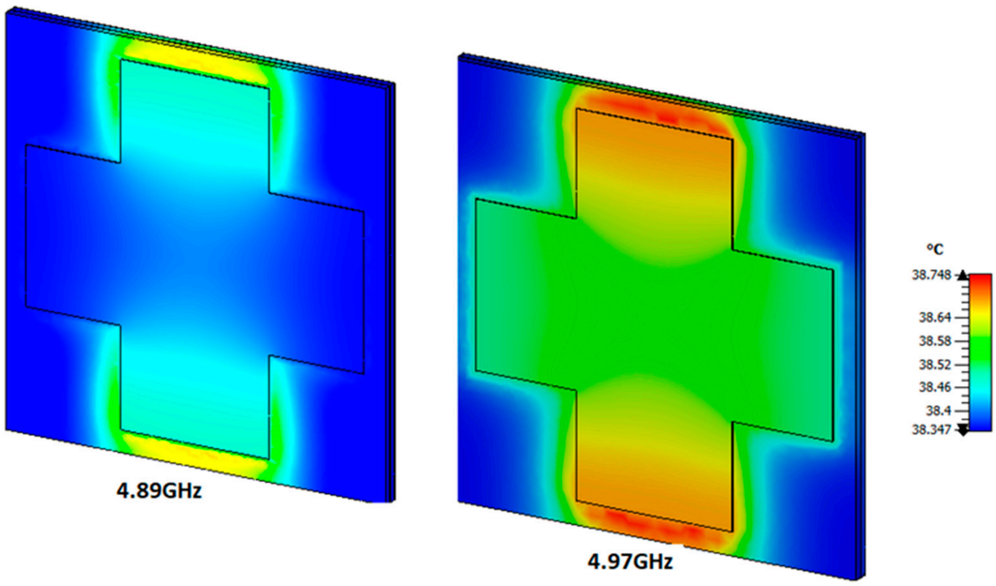

Figure 9. Simulated thermal distribution of the multilayer MA at the thermal equilibrium.

Apart from the electromagnetic wave absorption function of the proposed metamaterial structure, metamaterials have a lot of potential applications in other research directions, such as deep learning and machine learning applied in the design of circuit–analog plasmonic devices, all-optical neural networks, refractive-index sensors, metalenses, and coding metasurfaces [37–43]. The modulation capability of active metamaterial structures has also become a timely research interest [44,45]. Active elements were used to control the absorption frequency region of the metamaterial structure [46]. Optical modulators using the V-shape structure were also studied by Gardes et al. [47]. The metamaterial structure proposed in this paper can be attached to some external elements that control the absorption properties of structures. As we presented above, the horizontal capacitance between the crosses is currently very small and can be ignored. However, when we attach a capacitor or resistor to this gap, the frequency and absorption characteristics of the entire structure significantly change, depending on the value of the component. From there, the absorption properties of the structure can be actively manipulated.

4. Conclusions

We simulated, fabricated, and characterized a multilayer MA operating in the microwave region. The proposed structure consisted of two plus-shaped copper layers, placed at the top of the corresponding FR-4 dielectric layers and a continuous copper sheet at the bottom. The multilayer MA efficiently absorbed the incoming electromagnetic wave with an absorption greater than 90% in a frequency range from 4.84 to 5.02 GHz. The magnetic resonances in the individual layers and their coupling were the mechanisms of absorption, as indicated by the magnetic field and surface current distributions. The LC circuit model was used to calculate the resonant frequency, which showed good agreement with the absorption behavior. Widening the absorption bandwidth can be achieved by increasing the number of layers in the metamaterial structure. Upon increasing to three and four layers, the absorption bandwidth was augmented by 16% and 33%, respectively, compared to the suggested bilayer structure. Finally, the thermal distribution was also presented, which indicated that the temperatures of the MA reached 38.67 °C and 38.75 °C at frequencies of 4.89 and 4.97 GHz, respectively. Our work presents a strategy for the improved absorption properties of MAs by employing a multilayer structure. The implication of this approach can be extended beyond the microwave applications, encompassing the areas of electromagnetic shielding. This can also be developed for the design of MAs for THz technology, including emission and thermal imaging.

Author Contributions: Conceptualization, B.X.K. and N.N.V.; validation, B.S.T., N.H.A. and N.N.V.; formal analysis, D.T.C. and H.Z.; investigation, N.P.H., B.H.N. and P.T.S.; writing—original draft preparation, B.X.K.; writing—review and editing, Y.L., V.D.L. and L.C.; project administration, B.X.K. and Y.L. All authors have read and agreed to the published version of the manuscript.

Funding: This research was supported by the Excellent Research Team Development Program grant funded by the Vietnam Academy of Science and Technology (VAST), under grant no. NCXS02.01/23-24, and by the Korea Evaluation Institute of Industrial Technology (project no. 20016179).

Institutional Review Board Statement: Not applicable.

Informed Consent Statement: Not applicable.

Data Availability Statement: The data used and/or analyzed during the current study are available from the corresponding author upon reasonable request.

Conflicts of Interest: The authors declare no conflict of interest.

References

1. Smith, D.R.; Pendry, J.B.; Wiltshire, M.C.K. Metamaterials and Negative Refractive Index. *Science* **2014**, *305*, 788–792. [CrossRef]
2. Tong, S.; Ren, C.; Tang, W. High-transmission negative refraction in the gradient space-coiling metamaterials. *Appl. Phys. Lett.* **2019**, *114*, 204101. [CrossRef]
3. Singh, R.; Plum, E.; Menzel, C.; Rockstuhl, C.; Azad, A.K.; Cheville, R.A.; Lederer, F.; Zhang, W.; Zheludev, N.I. Terahertz metamaterial with asymmetric transmission. *Phys. Rev. B* **2009**, *80*, 153104. [CrossRef]
4. Cheng, Y.; Fan, J.; Luo, H.; Chen, F.; Feng, N.; Mao, X.; Gong, R. Dual-band and high-efficiency circular polarization conversion via asymmetric transmission with anisotropic metamaterial in the terahertz region. *Opt. Mater. Express* **2019**, *9*, 1365–1376. [CrossRef]
5. Cheng, H.; Chen, S.; Yu, P.; Li, J.; Xie, B.; Li, Z.; Tian, J. Dynamically tunable broadband mid-infrared cross polarization converter based on graphene metamaterial. *Appl. Phys. Lett.* **2013**, *103*, 223102. [CrossRef]
6. Zhu, W.; Yang, R.; Fan, Y.; Fu, Q.; Wu, H.; Zhang, P.; Shen, N.-H.; Zhang, F. Controlling optical polarization conversion with $Ge_2Sb_2Te_5$-based phase-change dielectric metamaterials. *Nanoscale* **2018**, *10*, 12054–12061. [CrossRef] [PubMed]
7. Landy, N.I.; Sajuyigbe, S.; Mock, J.J.; Smith, D.R.; Padilla, W.J. Perfect metamaterial absorber. *Phys. Rev. Lett.* **2008**, *100*, 207402. [CrossRef]
8. Chi, D.T.; Khuyen, B.X.; Tung, B.S.; Lam, V.D.; Chen, L.Y.; Lee, Y. Progresses in metamaterials for advanced low-frequency perfect absorbers: A brief review. *J. Electromagn. Waves Appl.* **2020**, *34*, 2251–2265. [CrossRef]
9. Hao, J.; Wang, J.; Liu, X.; Padilla, W.J.; Zhou, L.; Qiu, M. High performance optical absorber based on a plasmonic metamaterial. *Appl. Phys. Lett.* **2010**, *96*, 251104. [CrossRef]
10. Qu, S.; Hou, Y.; Sheng, P. Conceptual-based design of an ultrabroadband microwave metamaterial absorber. *Proc. Natl. Acad. Sci. USA* **2021**, *118*, e2110490118. [CrossRef]
11. Long, L.V.; Tung, N.H.; Giang, T.T.; Son, P.T.; Tung, N.T.; Tung, B.S.; Khuyen, B.X.; Lam, V.D. Rotary bi-layer ring-shaped metamaterials for reconfiguration absorbers. *Appl. Opt.* **2022**, *61*, 9078–9084. [CrossRef] [PubMed]
12. Tran, M.C.; Pham, V.H.; Ho, T.H.; Nguyen, T.T.; Do, H.T.; Bui, X.K.; Bui, S.T.; Le, D.T.; Pham, T.L.; Vu, D.L. Broadband microwave coding metamaterial absorbers. *Sci. Rep.* **2020**, *10*, 1810. [CrossRef]

13. Nguyen, T.K.T.; Cao, T.N.; Nguyen, N.H.; Bui, X.K.; Truong, C.L.; Vu, D.L.; Nguyen, T.Q.H. Simple design of a wideband and wide-angle insensitive metamaterial absorber using lumped resistors for X-and Ku-bands. *IEEE Photonics J.* **2021**, *13*, 1–10. [CrossRef]
14. Pham, T.L.; Dinh, H.T.; Le, D.H.; Bui, X.K.; Bui, S.T.; Dang, H.L.; Phan, D.A.; Le, D.T.; Vu, D.L. Dual-band isotropic metamaterial absorber based on near-field interaction in the Ku band. *Curr. Appl. Phys.* **2020**, *20*, 331–336. [CrossRef]
15. Phan, D.T.; Nguyen, T.K.T.; Nguyen, N.H.; Le, D.T.; Bui, X.K.; Vu, D.L.; Truong, C.L.; Nguyen, T.Q.H. Lightweight, ultra-wideband, and polarization-insensitive metamaterial absorber using a multilayer dielectric structure for C-and X-band applications. *Phys. Status Solidi B* **2021**, *258*, 2100175. [CrossRef]
16. Alaee, R.; Farhat, M.; Rockstuhl, C.; Lederer, F. A perfect absorber made of a graphene micro-ribbon metamaterial. *Opt. Express* **2012**, *20*, 28017–28024. [CrossRef]
17. Nguyen, T.Q.M.; Nguyen, T.K.T.; Le, D.T.; Truong, C.L.; Vu, D.L.; Nguyen, T.Q.H. Numerical study of an ultra-broadband and wide-angle insensitive perfect metamaterial absorber in the UV–NIR region. *Plasmonics* **2021**, *16*, 1583–1592. [CrossRef]
18. Le, D.T.; Tong, B.T.; Nguyen, T.K.T.; Cao, T.N.; Nguyen, H.Q.; Tran, M.C.; Truong, C.L.; Bui, X.K.; Vu, D.L.; Nguyen, T.Q.H. Polarization-insensitive dual-band terahertz metamaterial absorber based on asymmetric arrangement of two rectangular-shaped resonators. *Optik* **2021**, *245*, 167669. [CrossRef]
19. Ma, Y.; Chen, Q.; Grant, J.; Saha, S.C.; Khalid, A.; Cumming, D.R. A terahertz polarization insensitive dual band metamaterial absorber. *Opt. Lett.* **2011**, *36*, 945–947. [CrossRef]
20. Appasani, B.; Prince, P.; Ranjan, R.K.; Gupta, N.; Verma, V.K. A simple multi-band metamaterial absorber with combined polarization sensitive and polarization insensitive characteristics for terahertz applications. *Plasmonics* **2019**, *14*, 737–742. [CrossRef]
21. Li, L.; Yang, Y.; Liang, C. A wide-angle polarization-insensitive ultra-thin metamaterial absorber with three resonant modes. *J. Appl. Phys.* **2011**, *110*, 063702. [CrossRef]
22. Lu, G.; Wu, F.; Zheng, M.; Chen, C.; Zhou, X.; Diao, C.; Liu, F.; Du, G.; Xue, C.; Jiang, H.; et al. Perfect optical absorbers in a wide range of incidence by photonic heterostructures containing layered hyperbolic metamaterials. *Opt. Express* **2019**, *27*, 5326–5336. [CrossRef]
23. Nguyen, T.Q.H.; Nguyen, T.K.T.; Nguyen, T.Q.M.; Cao, T.N.; Phan, H.L.; Luong, N.M.; Le, D.T.; Bui, X.K.; Truong, C.L.; Vu, D.L. Simple design of a wideband and wide-angle reflective linear polarization converter based on crescent-shaped metamaterial for Ku-band applications. *Opt. Commun.* **2021**, *486*, 126773. [CrossRef]
24. Huynh, T.V.; Lam, V.D.; Khuyen, B.X.; Tung, B.S.; Tung, N.T. Controlling THz Absorption Properties of Metamaterials Based on Graphene. *J. Electron. Mater.* **2023**, *52*, 5719–5726. [CrossRef]
25. Ha, D.T.; Dzung, D.N.; Ngoc, N.V.; Tung, B.S.; Pham, T.S.; Lee, Y.; Chen, L.; Khuyen, B.X.; Lam, V.D. Switching between perfect absorption and polarization conversion, based on hybrid metamaterial in the GHz and THz bands. *J. Phys. D Appl. Phys.* **2021**, *54*, 234003. [CrossRef]
26. Othman, M.A.; Guclu, C.; Capolino, F. Graphene-based tunable hyperbolic metamaterials and enhanced near-field absorption. *Opt. Express* **2013**, *21*, 7614–7632. [CrossRef] [PubMed]
27. Liu, Y.; Zhang, B.; Duan, J.; Xu, Y. Flexible ultrawideband microwave metamaterial absorber with multiple perfect absorption peaks based on the split square ring. *Appl. Opt.* **2018**, *57*, 10257–10263. [CrossRef] [PubMed]
28. Liu, Y.; Ma, W.Z.; Wu, Y.C.; Meng, D.; Dou, C.; Cheng, Y.Y.; Chen, Y.S.; Liu, J.; Gu, Y. A metamaterial absorber with a multi-layer metal–dielectric grating structure from visible to near-infrared. *Opt. Commun.* **2023**, *542*, 129588. [CrossRef]
29. Quan, C.; Zou, J.; Guo, C.; Xu, W.; Zhu, Z.; Zhang, J. High-temperature resistant broadband infrared stealth metamaterial absorber. *Opt. Laser Technol.* **2022**, *156*, 108579. [CrossRef]
30. Gandhi, C.; Babu, P.R.; Senthilnathan, K. Ultra-thin polarization independent broadband terahertz metamaterial absorber. *Front. Optoelectron.* **2021**, *14*, 288–297. [CrossRef]
31. Liu, L.; Liu, W.; Song, Z. Ultra-broadband terahertz absorber based on a multilayer graphene metamaterial. *J. Appl. Phys.* **2020**, *128*, 093104. [CrossRef]
32. Odysseas, T.; Lei, Z.; Maria, K.; Costas, M.S.; Thomas, K. Experimental implementation of achromatic multiresonant metasurface for broadband pulse delay. *ACS Photonics* **2021**, *8*, 1649–1655.
33. Chen, X.; Grzegorczyk, T.M.; Wu, B.I.; Pacheco, J., Jr.; Kong, J.A. Robust method to retrieve the constitutive effective parameters of metamaterials. *Phys. Rev. E* **2004**, *70*, 016608. [CrossRef]
34. Zhou, J.; Economon, E.N.; Koschny, T.; Soukoulis, C.M. Unifying approach to left-handed material design. *Opt. Lett.* **2006**, *31*, 3620–3622. [CrossRef]
35. Cengel, Y.; Ghajar, A. *Heat and Mass Transfer: Fundamental and Applications*, 5th ed.; McGraw Hill Education: New York, NY, USA, 2015; pp. 79–80.
36. Ida, N. *Engineering Electromagnetics*, 3rd ed.; Springer Cham Publisher: Cham, Switzerland, 2015; pp. 625–626.
37. Xiong, J.; Shen, J.; Gao, Y.; Chen, Y.; Ou, J.Y.; Liu, Q.H.; Zhu, J. Real-time on-demand design of circuit-analog plasmonic stack metamaterials by divide-and-conquer deep learning. *Laser Photonics Rev.* **2023**, *17*, 2100738. [CrossRef]
38. Chen, R.; Li, Y.; Lou, M.; Fan, J.; Tang, Y.; Sensale-Rodriguez, B.; Yu, C.; Gao, W. Physics-aware machine learning and adversarial attack in complex-valued reconfigurable diffractive all-optical neural network. *Laser Photonics Rev.* **2022**, *16*, 2200348. [CrossRef]

39. Ma, X.; Ma, Y.; Preston, C.; Liu, Q.; Kaushik, K.; Xu, D.; Wang, J.; Chen, Y.; Wong, Z.J.; Liu, M.; et al. Strategical deep learning for photonic bound states in the continuum. *Laser Photonics Rev.* **2022**, *16*, 2100658. [CrossRef]
40. Silalahi, H.M.; Chiang, W.F.; Shih, Y.H.; Wei, W.Y.; Su, J.Y.; Huang, C.Y. Folding metamaterials with extremely strong electromagnetic resonance. *Photonics Res.* **2022**, *10*, 2215–2222. [CrossRef]
41. Hu, Q.; Zhao, J.; Chen, K.; Qu, K.; Yang, W.; Zhao, J.; Jiang, T.; Feng, Y. An intelligent programmable omni-metasurface. *Laser Photonics Rev.* **2022**, *16*, 2100718. [CrossRef]
42. Pan, Y.; Lan, F.; Zhang, Y.; Zeng, H.; Wang, L.; Song, T.; He, G.; Yang, Z. Dual-band multifunctional coding metasurface with a mingled anisotropic aperture for polarized manipulation in full space. *Photonics Res.* **2022**, *10*, 416–425. [CrossRef]
43. Zhao, F.; Li, Z.; Li, S.; Dai, X.; Zhou, Y.; Liao, X.; Cao, J.C.; Liang, G.; Shang, Z.; Zhang, Z.; et al. Terahertz metalens of hyper-dispersion. *Photonics Res.* **2022**, *10*, 886–895. [CrossRef]
44. Bao, L.; Cui, T.J. Tunable, reconfigurable, and programmable metamaterials. *Microw. Opt. Technol. Lett.* **2020**, *62*, 9–32. [CrossRef]
45. Wang, B.X.; Xu, C.; Duan, G.; Xu, W.; Pi, F. Review of broadband metamaterial absorbers: From principles, design strategies, and tunable properties to functional applications. *Adv. Funct. Mater.* **2023**, *33*, 2213818. [CrossRef]
46. Li, W.; Xu, M.; Xu, H.X.; Wang, X.; Huang, W. Metamaterial Absorbers: From tunable surface to structural transformation. *Adv. Mater.* **2022**, *34*, 2202509. [CrossRef]
47. Gardes, F.Y.; Tsakmakidis, K.L.; Thomson, D.; Reed, G.T.; Mashanovich, G.Z.; Hess, O.; Avitabile, D. Micrometer size polarisation independent depletion-type photonic modulator in Silicon On Insulator. *Opt. Express* **2007**, *15*, 5879–5884. [CrossRef]